35th Symposium on Naval Hydrodynamics
Nantes, France, July 7-July 12, 2022

Reynolds number and angle of attack effects on the flow over a 6:1 prolate spheroid

M. Plasseraud[1] and K. Mahesh[1]
([1] Department of Naval Architecture & Marine Engineering, University of Michigan, USA)

ABSTRACT

The flow around a 6:1 prolate spheroid is characterized by three-dimensional separations followed by coherent vortical systems. The study of such canonical geometry informs the behavior of more general vehicle dynamics and their dependence on Reynolds number and incidence. In this context, Large Eddy Simulation is performed on a 6:1 prolate spheroid for an incidence ranging from 10° to 90° and Reynolds number from 1×10^6 to 4×10^6. The results illustrate varying flow regimes depending on the two studied parameters. The different observed regimes are associated with variations in the topology of the recirculation, which leads to change in the loads.

INTRODUCTION

The flow around a 6:1 prolate spheroid is a canonical problem that displays many similarities with the flow around complex, immersed vehicles. One or several symmetric pairs of three–dimensional separations are commonly observed when the spheroid is at incidence, which lead to one or multiple pairs of coherent counter-rotating vortices (Fu et al., 1994). Ahn (1992) demonstrated the existence of a critical Reynolds number between $Re = U_0 L/\nu = 2M$ and $Re = 3M$ (where L is the length of the spheroid, ν is the kinematic viscosity, U_0 is the freestream velocity) at $\alpha = 10^\circ$ and $\alpha = 20^\circ$ that separates a regime characterized by laminar, early separation on the side of the spheroid, to a regime of turbulent, delayed separation. This transition is associated with change in the location of the separation line, the angle of the separated sheet and the topology of the vortex. In addition to a critical Reynolds number, the Direct Numerical Simulations (DNS) of the spheroid at $Re = 1.8 \times 10^4$ at $\alpha = 45^\circ$ performed by Jiang et al. (2015) demonstrated the presence of an asymmetric wake at sufficiently high angle of attack. Similarly, El Khoury et al. (2010) observed an alternate shedding at a Strouhal number of 0.156 for the prolate spheroid at $\alpha = 90^\circ$ and $Re = 6 \times 10^4$. At such extreme angle of attack, the separation is two–dimensional while it was shown to be three–dimensional for smaller incidence of 10° and 20° (Plasseraud et al., 2023). This study suggested that the complex pressure gradient and curvature effects exist on the windward side of the prolate spheroid, increasing with incidence. These effects lead to a partial stabilization of the tripped boundary leading to a primary separation at $Re = 4.2 \times 10^6$ that is perturbed though not fully turbulent. In addition, the authors proposed a partition of the near-wall spheroid flow based on a skin-friction versus x/L and ϕ map, which identifies several regions of unique physical mechanisms including separations, reattachments, turbulent transition and relaminarization.

In addition to a critical Reynolds number, these studies suggest the existence of one or several critical angles of attack that separate a regime of symmetric, three-dimensional vortices to a regime of alternate shedding similar to what is observed on the flow around a cylinder. These changes in the vortical structure are associated with changes in the static and dynamic loads of the flow onto the spheroid. Characterizing the evolution of the loads on the spheroid is of critical importance to understand the maneuverability of smooth blunt bodies. The goal of this study is classify the regime of separation and the topology of the recirculation region for a large range of angles of attack and across the turbulent transitional Reynolds number.

NUMERICAL DETAILS

The LES solves the filtered incompressible Navier–Stokes equations using the algorithm developed by Mahesh et al. (2004) for unstructured grids on massively parallel platforms. The spatially-filtered incompressible

Navier–Stokes equation are:

$$\frac{\partial \overline{u}_i}{\partial t} + \frac{\partial}{\partial x_j}(\overline{u}_i \overline{u}_j) = -\frac{\partial \overline{p}}{\partial x_i} + \nu \frac{\partial^2 \overline{u}_i}{\partial x_j \partial x_j} - \frac{\partial \tau_{ij}}{\partial x_j} \quad (1)$$

$$\frac{\partial \overline{u}_i}{\partial x_i} = 0 \quad (2)$$

where u_i is the velocity, p is the pressure and ν is the kinematic viscosity. The overbar $\overline{(\cdot)}$ denotes spatial filtering and $\tau_{ij} = \overline{u_i u_j} - \overline{u}_i \overline{u}_j$ is the subgrid stress, which is modeled using the dynamic Smagorinsky model (Germano et al., 1991; Lilly, 1992). The algorithm uses a finite volume method where the Cartesian velocity components and pressure are stored at the centroids of the control volumes, while the face normal velocities are stored independently at the centroids of the faces. Time marching is performed using a Crank–Nicholson differencing scheme. The equations are discretized in space with a second order central scheme.

The angle of attack α is taken at 10°, 20°, 30°, 50°, 70° and 90°. The Reynolds number based on the semi-major axis of the spheroid L and the free-stream velocity U_0 is chosen at $Re = 1M$, $2M$, $3M$ and $4M$. This is sufficient to span the critical regime. The azimuthal coordinate ϕ originates on the windward meridian and increases until $\phi = 180°$ on the leeward meridian. The x-axis is taken along the major length of the spheroid; the y-axis points from the windward side to the leeward side; the z-axis is in the spanwise direction. Numerically and experimentally, the flow is tripped at the nose of the spheroid to obtain a turbulent boundary layer and guarantee more predictable flow behavior. In the current study, a normal velocity of $0.05U_0$ is prescribed at $x/L = 0.2$. The considered grid is made of 200 million hexahedral cells split among three overset volumes. Even though the geometry is static, an overset approach is used to circumvent the need for a 1:1 cell match between the near-wall and the far-field. An additional overset volume is used on the leeward side of the flow, to obtain a better resolution of the recirculation region. The domain is a cylinder of 20 spheroid diameter length and 16 spheroid diameter radius. The Dirichlet boundary condition is prescribed at the inflow with a uniform velocity U_0; and a Neumann conditional at the outflow and on the sides. For each of the cases, the simulation is run for two flow-through, at which point to flow becomes statistically steady. The flow statistics are then collected for a minimum of one flow through.

RESULTS AND DISCUSSION

Effect of angle of attack

Figure 1 shows a perspective view of the flow for $Re = 1M$ and the six angles of incidence considered, colored by mean axial vorticity. At $\alpha = 10°$, a single pair of coherent counter-rotating vortices is observed, formed around mid–body and preserved downstream of the spheroid. Similarly at $\alpha = 20°$, a coherent pair is observed, as well as a secondary pair closer to the wall (opposite color as the primary pair). The separated flow from the trailing edge merges with the primary vortex in the downstream of the vortex. The axial vorticity is stronger and the vortex appears more upstream compared to the 10° case. The flow at 30° for $x/L > 0.5$ is similar to the one at 20°. Downstream, a second primary vortex separates from the wall and merges with the primary vortex from the upstream part. Similarly to 10° and 20°, a single coherent counter-rotating vortex pair is visible in the wake, however, the size of that vortex increases downstream of the tail. The increase in size of the counter-rotating vortex pair is amplified in the $\alpha = 50°$ case and is accompanied with a decrease of the axial vorticity in the streamwise direction. The increase in size can be understood as a shedding of coherent by the freestream once the vortex pair is downstream of the tail: at small angle of attack, the axis of the vortex is nearly aligned with the freestream and the separated vortex is accelerated along its axis; at large angle of attack, the freestream velocity vector has a significant component in the direction orthogonal to the vortex axis, the vortex pair is sheared and loses coherence. At $\alpha = 70°$ and $\alpha = 90°$, the vortex pair is not clearly visible and the leeward separation resembles a turbulent wake.

Figure 3 shows the instantaneous velocity magnitude at the six considered angles of attack, at Re = 1M. At 10°, the boundary layer is unsteady both on the windward side and at the separation, which indicates that the trip is effective even at the lowest Reynolds number considered. This behavior was previously observed in Plasseraud et al. (2023) where it was discussed that at that low angle of attack, the tripping was effective while ineffective for the 20° case. The recirculation region on the leeward side is small, close to the wall and unsteady. The boundary layer separates at around $\phi = 110°$. For $\alpha > 10°$, the separation is laminar although the separation sheet and recirculation area are unsteady. The azimuths of separation for these cases are all smaller than the 10° case. At $\alpha = 20°$, the coherent counter-rotating vortices are visible, in addition to small secondary vortices below the former. The velocity in the recirculation area is smaller than that of the freestream. The $\alpha = 30°$ shows similar coherent counter-rotating vortices with notable differences compared to the 20° case: the vortices are larger in both directions, the angle of the separated sheet is wider, the velocity in the vortex is larger than the free-stream. At $\alpha = 50°$, the vortex pair becomes even larger than the 30° case, albeit mostly in the y direction. At $\alpha = 70°$, no coherent vortex pair is observed in the instantaneous fields, the leeward flow resembles a wake

flow. That region is narrower than the $\alpha = 50^\circ$ case with a larger momentum deficit and a smaller angle of the separation sheet. At $\alpha = 90^\circ$, the angle of separation is similar although the wake flow has a strong asymmetry that suggests alternate shedding.

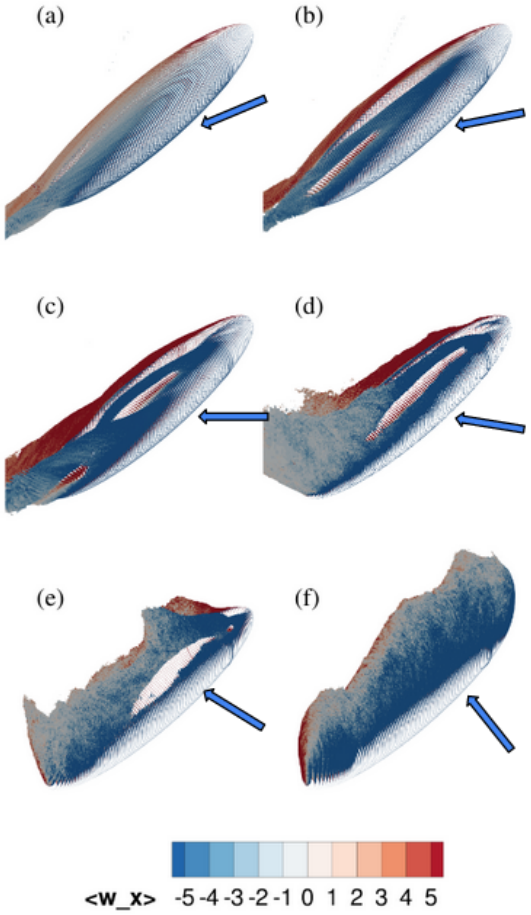

Figure 1: Perspective view of the flow around the prolate spheroid for $Re = 1M$, $\alpha = 10^\circ$ (a), $\alpha = 20^\circ$ (b), $\alpha = 30^\circ$ (c), $\alpha = 50^\circ$ (d), $\alpha = 70^\circ$ (e) and $\alpha = 90^\circ$ (f). The color represents the time-averaged axial vorticity. The view is kept at constant angle with the spheroid for ease of comparison.

Figure 2 shows the skin friction coefficient for the six angles of attack, for $Re = 1 \times 10^6$. The primary separation is visible as a line of decreasing c_f ($\alpha \geq 20^\circ$) and rotation of the friction line (($\alpha = 10^\circ$). The primary separation is turbulent for $\alpha = 10^\circ$ and laminar for $\alpha \geq 20^\circ$. For $\alpha = 20^\circ$ and $\alpha = 30^\circ$, the separation line is relatively straight while it shows oscillations for $\alpha \geq 50^\circ$. These oscillations suggest that the location of the separation is not constant in time. A secondary separation is observed for the $\alpha = 20^\circ, 30^\circ$ and 50° cases. It is unclear whether secondary separation occurs for the 70° and 90° cases. For the 10° case only, the flow is unsteady for all azimuthal location downstream of the trip. On the other hand, for $\alpha \geq 20^\circ$, the flow is unsteady directly downstream of the trip and downstream of the primary separation while it is laminar upstream of separation. Some streamwise perturbations are nonetheless observed on the windard side for $\alpha \geq 20^\circ$, as discussed in Plasseraud et al. (2022, 2023). Overall, the skin friction coefficient increases on the windward side with angle of attack. Relaminarization is observed upstream of secondary separation in the $\alpha = 20^\circ, 30^\circ$ and 50°.

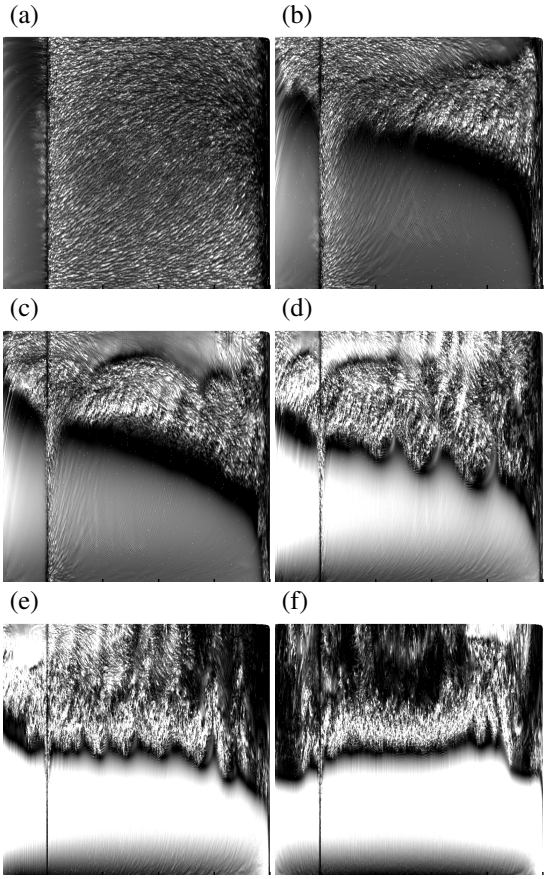

Figure 2: Skin friction coefficient c_f versus x/L and ϕ, for $Re = 1M$, $\alpha = 10^\circ$ (a), $\alpha = 20^\circ$ (b), $\alpha = 30^\circ$ (c), $\alpha = 50^\circ$ (d), $\alpha = 70^\circ$ (e) and $\alpha = 90^\circ$ (f).

Figure 4 shows the time-averaged stagnation pressure $\langle P_s \rangle = \langle P + 1/2 u_i u_i \rangle$ and the time-averaged secondary streamlines for the six angles of attack considered, at $Re = 1M$ and $x/L = 0.8$. The primary vortex pair becomes progressively bigger from $\alpha = 10^\circ$ to $\alpha = 50^\circ$. For the 10° case, the vortex is close to the wall, elongated and non-axisymmetric. At 20°, the vortex is more circular, has similar size in the z-direction

as the previous case although more than twice the size in the y-direction. A closed isoline of stagnation pressure indicates the core of the vortex (Plasseraud and Mahesh, 2024). At 30°, the secondary streamlines show that the separation is much larger than at 20°. The stagnation pressure indicates that the separation is made of two distinct co-rotating vortex core. At 50°, at this location, a single pair of primary vortices is observed. The size of the recirculation in the z-direction is similar as the 30° case and stretched in the y-direction. At $\alpha = 70°$ and $\alpha = 90°$, the stagnation pressure confirms the observation of Figure 3 that primary vortex loses coherence and that the recirculation region is wake-like.

Effect of Reynolds number

Figure 5 shows the time–averaged stagnation pressure at $x/L = 0.8$ for the four considered Reynolds numbers, at $\alpha = 30°$. The case with the lower Reynolds number has an early separation, a wider separation angle with a recirculation region that is larger in the z-direction though narrower in the y-direction. The stagnation pressure in the core of the vortex is similar as the other, higher Reynolds number cases. The $Re = 2M$, $3M$ and $4M$ are very similar and show a coherent primary vortex pair with a counter-rotating secondary pair. The angle of separation and the distance between the cores are slightly larger between the $2M$ case and the $3M$ case. These observation suggest that the boundary layer separation is laminar for the $1M$ case, transitional in the $2M$ case and turbulent in the $3M$ and $4M$ cases.

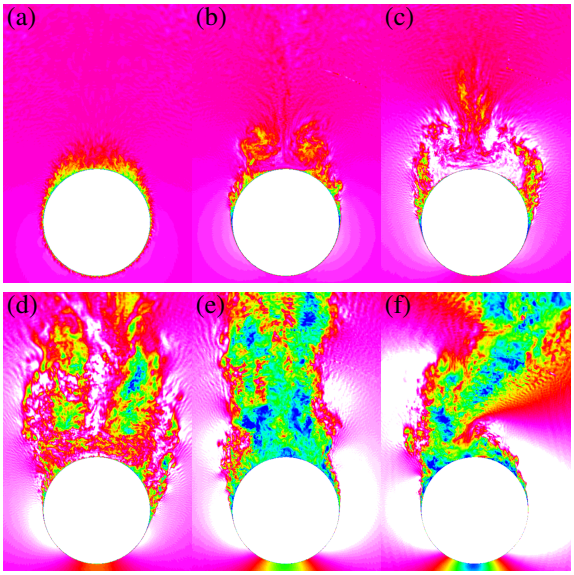

Figure 3: Instantaneous velocity magnitude at $x/L = 0.8$, for $Re = 1M$, $\alpha = 10°$ (a), $\alpha = 20°$ (b), $\alpha = 30°$ (c), $\alpha = 50°$ (d), $\alpha = 70°$ (e) and $\alpha = 90°$ (f)

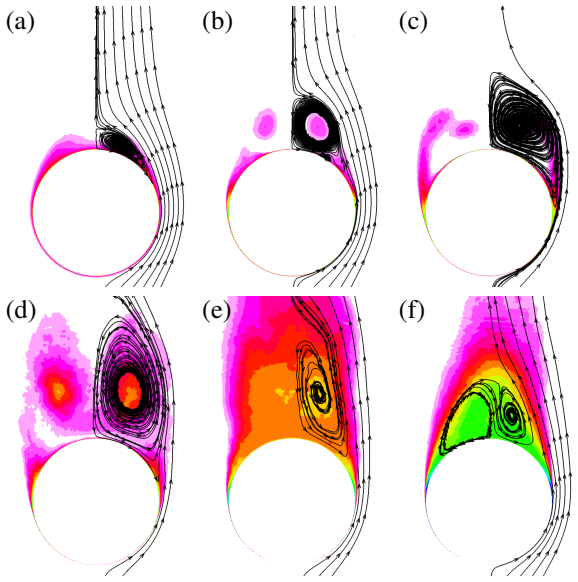

Figure 4: Averaged stagnation pressure and secondary streamlines at $x/L = 0.8$, for $Re = 1M$, $\alpha = 10°$ (a), $\alpha = 20°$ (b), $\alpha = 30°$ (c), $\alpha = 50°$ (d), $\alpha = 70°$ (e) and $\alpha = 90°$ (f)

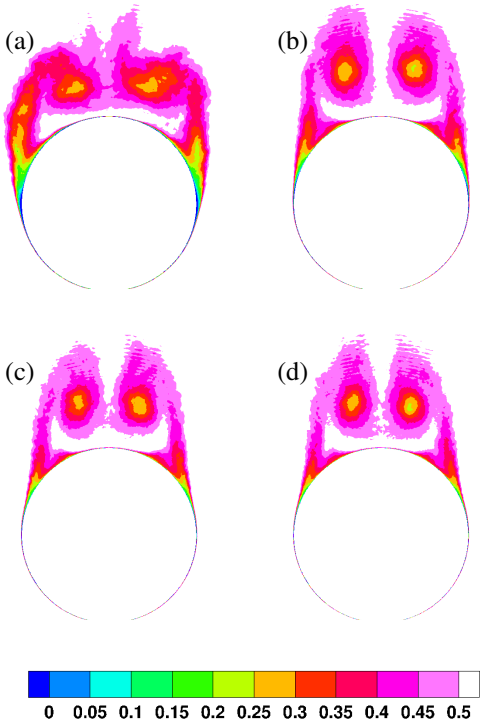

Figure 5: Averaged stagnation pressure and secondary streamlines at $x/L = 0.8$, for $\alpha = 30°$, $Re = 1M$ (a), $Re = 2M$ (b), $Re = 3M$ (c) and $Re = 4M$ (d)

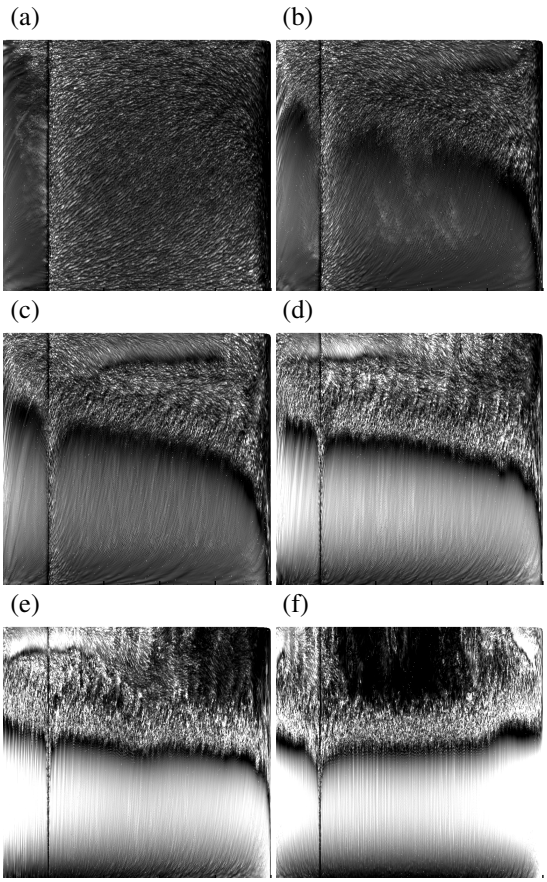

Figure 6: Skin friction coefficient c_f versus x/L and ϕ, for $Re = 2M$, $\alpha = 10^\circ$ (a), $\alpha = 20^\circ$ (b), $\alpha = 30^\circ$ (c), $\alpha = 50^\circ$ (d), $\alpha = 70^\circ$ (e) and $\alpha = 90^\circ$ (f).

Figure 6 show the skin friction coefficient for the six angles of attack at $Re = 2 \times 10^6$. Similarly to Figure 2, the primary separation is visible as a line of minimum c_f, although it is more perturbed, indicating a change of regime with increasing Reynolds number. A secondary separation is also observed for $\alpha \in [20^\circ, 90^\circ]$ at $\phi \approx 170^\circ$. The axial location of this separation line decreases with the incidence. At $\alpha = 90^\circ$, one secondary separation line is visible at each tip of the spheroid. At this incidence, a large region of low skin friction is also observed on the midbody, in the leeward side. The skin friction is locally maximum at the center of this region at $x/L = 0.5$ and $\phi = 180^\circ$. This location corresponds to a point of reattachment of the primary separation and subsequent radial flow. Similar low skin friction areas are observed on the tail of the spheroid at $\alpha = 50^\circ$ and 70° albeit not as pronounced. These low friction regions are interpreted as areas of low velocity that are not under a coherent vortex. In comparison to the $Re = 1 \times 10^6$ case, the wavelength of the unsteadiness is smaller, the separation lines are more defined, without the oscillations observed in Figure 2. The perturbations on the windward side are stronger in the $Re = 2 \times 10^6$ compared to the $Re = 1 \times 10^6$ case.

Relation with the loads

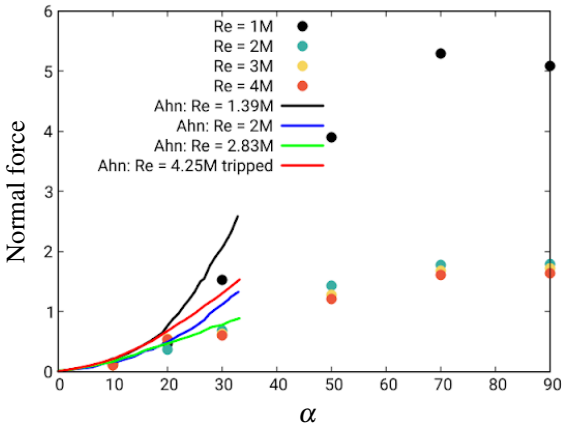

Figure 7: Normal force versus angle of attack for the four Reynolds number considered, compared with Ahn (1992).

Figure 7 shows the evolution of the normal force with the angle of attack. For the four Reynolds numbers considered, the loads increase with angle of attack from $\alpha = 10^\circ$ to $\alpha = 70^\circ$, and are close to constant from $\alpha = 70^\circ$ to $\alpha = 90^\circ$. The increase of the normal force is associated with the previously discussed increase of the recirculation region. The force is the highest for the $Re = 1M$ case and is increasingly largest with increasing incidence. Similarly, the force at $Re = 2M$ is slightly larger than the $3M$ and $4M$ cases.

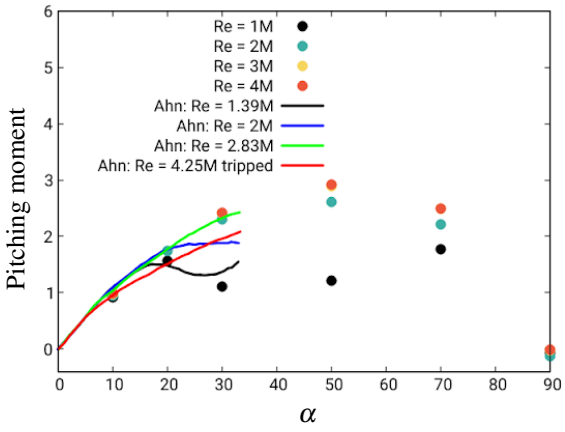

Figure 8: Pitching moment versus angle of attack for the four Reynolds number considered, compared with Ahn (1992).

Figure 8 shows the evolution of the spanwise moment with the angle of attack for the four Reynolds

numbers considered. Apart from the $Re = 1M$, the spanwise moment increases with the incidence to reach a maximum at $\alpha = 50^\circ$, then decreases to zero at $\alpha = 90^\circ$. The moment in the $Re = 1M$ case is locally minimum at $\alpha = 30^\circ$ and $\alpha = 50^\circ$. Unlike the normal force, the spanwise moment increase with Reynolds number, with the $Re = 2M$ case also being slightly smaller than the $Re = 3M$ and $Re = 4M$ cases.

Regimes of flow

Four regimes are identified depending on the angle of attack

- For the lowest angle of attack, the recirculation has no core and no rotation center, instead, separated streamlines lose their azimuthal velocity and curve in the axial direction.

- At 20° and 30° incidence, a single primary vortex is formed with a distinct core. The vortex is attached, which means that a separated sheet extends from the separation line on the wall, to the core. A secondary vortex, rotating in the opposite direction is also visible

- From 30° to 50°, the primary vortex is made of several independent co-rotating vortices. Unlike the previous case, each primary vortex segment does not extend to the entire length of the spheroid, instead the vortex segments are attached for the first part and separate on a downstream portion. A new vortex segment starts at the location where the previous segments detaches. Both the separated and attached segments are co-rotating and merge.

- For $\alpha \geq 70^\circ$, the separation area is large and does not form a single vortex instead forms a wake. No coherent rotating flow is observed.

The following effect of Reynolds number was observed, independently of the angle of incidence:

- At $Re = 1 \times 10^6$, the boundary is laminar at separation. The separated sheet becomes unsteady before roll-up into the primary vortex;

- At $Re = 2 \times 10^6$, the boundary layer is transitional at separation;

- At $Re \geq 3 \times 10^6$, the boundary layer is fully turbulent, the separation is delayed compared to lower Reynolds number and similar for both $Re = 3 \times 10^6$ and $Re = 4 \times 10^6$. The separation sheet angle is smaller, leading to a smaller recirculation area and smaller loads.

CONCLUSION

Large-eddy simulation of the prolate spheroid flow was performed for a range of Reynolds number from $Re = 1M$ to $Re = 4M$ and angles of attack from $\alpha = 10^\circ$ to $\alpha = 90^\circ$. For all the considered cases, three–dimensional separation occurs and leads to a large recirculation region. Several regimes were identified depending on the two considered parameters. For every angle of attack considered, the separation is laminar for the lowest Reynolds number with a large vortex pair and strong normal force. The separation is turbulent for the two highest Reynolds number with delayed separation, smaller separation angle leading to a narrower recirculation area and normal force. At small to moderate angle of attack, the primary vortices are coherent. They increase in size with incidence leading to a larger normal force. Starting from $\alpha = 70^\circ$, the vortex pair loses coherence, the recirculation turns into a wake flow and the normal force does not change with the incidence.

ACKNOWLEDGEMENTS

This work is supported by the United States Office of Naval Research under ONR Grant N00014-20-1-2717 with Dr. Peter Chang as technical monitor. Computing resources were provided through a United States Department of Defense (DoD) Frontier project of the High Performance Computing Modernization Program (HPCMP) by the US Army Engineer Research and Development Center (ERDC) in Vicksburg, Mississippi.

REFERENCES

Ahn, S. An experimental study of flow over a 6 to 1 prolate spheroid at incidence. PhD thesis, Virginia Polytechnic Institute and State University, 1992.

El Khoury, George K, Andersson, Helge I, and Pettersen, Bjørnar. "Crossflow past a prolate spheroid at reynolds number of 10000". Journal of fluid mechanics, 659: 365–374, 2010.

Fu, T. C., Shekarriz, A., Katz, J., and Huang, T. T. "The flow structure in the lee of an inclined 6:1 prolate spheroid". Journal of Fluid Mechanics, 269:79–106, 1994.

Germano, M., Piomelli, U., Moin, P., and Cabot, W. H. "A dynamic subgrid–scale eddy viscosity model". Physics of Fluids A, 3:7:1760, 1991.

Jiang, Fengjian, Gallardo, José P, Andersson, Helge I, and Zhang, Zhiguo. "The transitional wake behind an inclined prolate spheroid". Physics of Fluids, 27(9), 2015.

Lilly, D. K. “A proposed modification of the Germano subgrid–scale closure model”. Physics of Fluids A, 4:3: 633, 1992.

Mahesh, Krishnan, Constantinescu, George, and Moin, Parviz. “A numerical method for large-eddy simulation in complex geometries”. Journal of Computational Physics, 197(1):215–240, 2004.

Plasseraud, M, Kumar, P, Ma, R, and Mahesh, K. “Simulation of flow over an inclined spheroid at high reynolds number: tripping effects”. In Proceedings of the 34^{th} Symposium on Naval Hydrodynamics, 2022.

Plasseraud, Marc and Mahesh, Krishnan. “Definition of vortex boundary using stagnation pressure”. arXiv preprint arXiv:2404.18987, 2024.

Plasseraud, Marc, Kumar, Praveen, and Mahesh, Krishnan. “Large-eddy simulation of tripping effects on the flow over a 6: 1 prolate spheroid at angle of attack”. Journal of Fluid Mechanics, 960:A3, 2023.